Low phonon thermal conductivity of layered $(Bi_2)_m$-$(Bi_2Te_3)_n$ thermoelectric alloys

P. A. Sharma,[1] A. L. Lima Sharma,[1,2] D. L. Medlin,[1] A. M. Morales,[1] N. Yang,[1] M. Barney,[1] J. He,[3] F. Drymiotis,[3] J. Turner,[3] and T. M. Tritt[3]

[1]*Sandia National Laboratories, 7011 East Avenue, Livermore, California 94550, USA*

[2]*Department of Physics and Astronomy, San Jose State University, San Jose, California 95192, USA*

[3]*Department of Physics and Astronomy, Clemson University, Clemson, South Carolina 29634-0978, USA*

(Received 2 February 2011; revised manuscript received 31 March 2011; published 14 June 2011)

We examined the thermal conductivity of the $(Bi_2)_m$-$(Bi_2Te_3)_n$ alloys, which are composed of alternating sequences of Bi_2 and Bi_2Te_3 structural units. The phonon thermal conductivity of these alloys was sharply reduced relative to that of elemental Bi and Bi_2Te_3 for temperatures below 100 K. Our measurements suggested that defects reduce the thermal conductivity in these materials. Using the Debye-Callaway model for heat transport, we link this reduced thermal conductivity to point defects.

DOI: 10.1103/PhysRevB.83.235209 PACS number(s): 66.70.Df, 72.20.Pa, 61.72.J−

I. INTRODUCTION

The phonon thermal conductivity κ_P of thermoelectric alloys should be reduced as much as possible in order to increase the efficiency of thermoelectric devices.[1] Understanding how a low κ_P occurs in different thermoelectric materials is also an interesting problem in phonon transport. In some bulk alloys, such as the skutterudites, "rattling" guest atoms in the open spaces of the crystal structure are thought to strongly scatter phonons,[2] thus lowering κ_P. Strong bond anharmonicity[3] and nanostructuring[2] may also increase phonon scattering. In general, crystal structure, the nature of atomic bonding, and microstructure will all influence κ_P at the same time.[4,5] Understanding why certain thermoelectric materials have low κ_P then amounts to uncovering the dominant phonon-scattering mechanism.

Bi_2Te_3 is one of the best thermoelectric materials due to its low κ_P. One can combine excess Bi with Bi_2Te_3 and form a series of intermetallic phases,[6] where excess metal ions form in charge-neutral bilayers interleaved between Bi_2Te_3 blocks.[7] Depending on the amount of excess Bi, many different layered structures are possible. Materials with layered crystal structures often have a reduced κ_P,[8,9] originating from interface scattering or changes in phonon band structure in analogy to artificial superlattices.[10] It is therefore interesting to see if κ_P changes systematically with the "superlattice" structure of the $(Bi_2)_m$-$(Bi_2Te_3)_n$ series or whether other mechanisms dominate the thermal transport in this system.

While both the Seebeck coefficient and resistivity ρ have been measured for several $(Bi_2)_m(Bi_2Te_3)_n$ compounds,[7] κ_P has not been reported and is the focus of the present work. Here, we found that while these alloys had a reduced κ_P relative to elemental Bi and Bi_2Te_3 below 100 K. The κ_P reduction did not change systematically with Bi content, even though the stacking sequence of Bi bilayer and Bi_2Te_3 structural units had changed, because our measurements were only sensitive to the in-plane thermal conductivity of these materials. Using calorimetry, we inferred that κ_P must be reduced from a decrease in the phonon mean free path, which suggests that microscopic defects increase phonon scattering. We used the Debye-Callaway approximation of the Boltzmann equation to model κ_P based on the hypothesis that defects increase phonon scattering. In this way, point defects were linked to the reduction of κ_P. The magnitude of the point defect scattering rate suggested that vacancies or antisite defects, at concentrations of 2%–6%, were the relevant point defects in these materials.

II. SYNTHESIS

We prepared samples of $(Bi_2)_m$-$(Bi_2Te_3)_n$ in two different ways in order to control the grain size and porosity of the material used for measurements. The reasons for these control experiments are further explained in Sec. V and VI.

In the first method, we prepared Bi_2Te_3, Bi_2Te, BiTe, and Bi_6Te_7 using solid-state reaction routes previously reported by Bos *et al.*[7] Stoichiometric amounts of powder Bi_2Te_3 (99.99%) and Bi (99.99%) obtained from Alfa Aesar were mixed and ground together in an agate mortar. The mixed powders were pressed into 13-mm pellets under a load of 3000 pounds and sealed in quartz tubes under 100 Torr of hydrogen. The samples were sintered under the following conditions: Bi_2Te_3 at 525 °C, Bi_6Te_7 at 485 °C, BiTe at 430 °C, and Bi_2Te at 285 °C, each for 2 days. Sintering temperatures were chosen based on the equilibrium phase diagram.[6] The resulting pellets were checked for phase purity and the correct lattice parameters, as compared to Bos *et al.*,[7] using powder x-ray diffraction (XRD). These pellets were then reground for consolidation using spark plasma sintering (SPS) using a Dr. Sinter, SPS-515S unit. In this technique, precursor powders are sintered at low temperature, under pressure and high electric currents. SPS samples were prepared from both sieved and unsieved prereacted powders for reasons described later. Powders for SPS consolidation were loaded into a 13-mm graphite die coated with BN, which avoided loss of current from the sample to die and contamination. For each sample, current was injected through the die/sample at 100 A/min under pressure. A drastic change in piston displacement indicated that sintering had begun, at which point the current (and sintering temperature) was kept constant for 10 min before furnace cooling (∼15 min) to room temperature. The SPS conditions for each sample were Bi_2Te_3: 175 A, 350 C; BiTe: 150 A, 350 C; Bi_2Te: 100 A, 250 C; and Bi_6Te_7: 200 A, 360 C. All samples were loaded with a force of 5 kN. Phase purity and lattice parameters

were unchanged after the SPS step. Phase purity was further checked using transmission electron microscopy (TEM) after SPS processing. We used this SPS route because we found that porosity could be greatly reduced and grain size did not change from that of the precursor powder.

In the second method of preparation, we synthesized Bi_4Te_3 from the melt in order to achieve large grain sizes. The Bi_4Te_3 sample was prepared by melting stoichiometric amounts of Bi (99.99%) and Te (99.99%) from Alfa Aesar in an evacuated quartz tube at 700 C. The melt was quenched from 700 C in liquid nitrogen, then annealed at 400 C for 2 weeks. After annealing, this sample was found to be phase pure through x-ray diffraction and TEM microscopy. We were not able to grow large single crystals at the time of this writing, so all measurements reported are on polycrystalline specimens.

III. MEASUREMENTS

We conducted transmission electron microscopic (TEM) observations of these materials using a JEOL 2010F instrument (JEOL Ltd., Japan) operated at 200 keV. Samples were prepared for TEM observation by mechanical dimpling followed by Ar+ ion milling in a liquid-nitrogen-cooled ion mill (Fischione, Model 1010).

The phase purity and lattice parameters of all samples were obtained by x-ray powder diffraction using a Scintag diffractometer with Cu-$K\alpha$ radiation fitted with an HPGe planar photon detector. Grain size and texture measurements were conducted using electron backscatter diffraction (EBSD) contrast in an SEM. Qualitative metallography was performed on polished samples in an optical microscope.

We used the thermal transport option of the physical property measurement system (PPMS, Quantum Design) for κ and ρ measurements. These measurements were conducted under high vacuum. Low resistance ohmic contacts were achieved by first polishing the sample surface down to 800 grit, then electroplating nickel contact pads. Electrical leads (gold plated copper) were fixed to the nickel contacts using EPO-TEK H20B silver epoxy. The dimensions of each sample were kept constant ($\sim 2 \times 2 \times 7\text{mm}^3$). Radiation errors in the thermal conductivity were negligible in the low-T region ($<$100 K) of interest. The heat-capacity option of the PPMS was used to obtain specific-heat (C) measurements using a relaxation method down to 2 K.

IV. STRUCTURE OF $(Bi_2)_m$-$(Bi_2Te_3)_n$ ALLOYS

Figure 1 shows the crystal structures of BiTe, Bi_2Te, and Bi_6Te_7 compared to Bi_2Te_3. Each compound is made up of alternating layers of Bi_2Te_3 and Bi_2 subunits. The evidence for this structural model is summarized in Ref. 7.

To confirm the phase identification for our compounds, we analyzed the materials using selected area electron diffraction on individual single-crystal grains in the TEM, while lattice parameters were calculated from bulk powder XRD patterns. The lattice constants for the prepared Bi-Te phases were obtained by first modeling the reported structures for these compounds using Crystal Maker® (CrystalMaker Software Ltd, Oxford, England, www.crystalmaker.com); generating a simulated XRD powder pattern for each compound using Crystal Diffract (also from CrystalMaker Software); and then using the simulated peak positions and *hkl* index assignments to assign *hkl* indexes to the x-ray data. Lattice parameters were then determined using Cohen's method for noncubic systems,[11] and agreed with those found by Bos *et al.*[7]

Selected area electron-diffraction patterns (Fig. 1) collected in the TEM were further used to identify each phase using the indexing scheme discussed in Ref. 7. This indexing scheme allows diffraction data from different structures within the compositional series to be unambiguously compared as perturbations of a single, simple unit cell. Specifically, the structures in the $(Bi_2)_m(Bi_2Te_3)_n$ series are referenced to a hypothetical rhombohedral subcell with *abc* stacking (space group $R\bar{3}m$). This subcell ($a \sim 4.4$ Å and $c \sim 6.0$ Å in the hexagonal setting) is chosen to give the primary diffraction reflections associated with the short-range periodicities of the crystal structure, but not the additional superlatticelike reflections that are associated with the long-range compositional and structural modulations, which vary as a function of Bi fraction. Distortions relative to this idealized structure are described by introducing an additional "modulation vector," $\mathbf{q} = \gamma[0001]^*$.

The modulation vector is denoted by an index m, which is added to the conventional $\{hk(i)l\}$ reciprocal-space indexing [i.e., $\{hk(i)l;m\}$]. The positions of the superlattice reflections are then given by linear combinations (in reciprocal space) of the reflections of the reference lattice, characterized by the index l, and the modulation vector multiplied by m. Along the $\{000l\}$ row in the diffraction pattern, these positions are $g_{l;m} = g_{3;0}(m\gamma + l)/3$. We have used this indexing approach to characterize the diffraction patterns obtained from our materials. We measured the peak positions along the $\{000l\}$ rows of selected area electron-diffraction patterns obtained from $\langle 2\bar{1}\bar{1}0\rangle$ or $\langle 10\bar{1}0\rangle$ oriented grains. The peak positions were normalized by the distance to the $\{0003;0\}$ reflection ($g_{3;0}$) to eliminate errors due to uncertainty in the instrumental camera-length calibration. For each pattern, we computed γ for each observed reflection between $\{000\text{-}3;0\}$ and $\{0003;0\}$ from $\gamma = \left(3g_{l;m}/g_{3;0} - 1\right)/m$. The γ values reported in Fig. 1 were averaged from at least three separate grains and agreed within one standard deviation to the γ values found in Ref. 7. In summary, our XRD and TEM diffraction experiments confirm that each sample was phase pure and had the expected crystal structures as shown in Fig. 1.

V. PHONON THERMAL CONDUCTIVITY OF $(Bi_2)_m(Bi_2Te_3)_n$ ALLOYS

We measured κ_P (Fig. 2) for Bi_2Te, BiTe, and Bi_6Te_7 and compared the results to Bi_2Te_3, prepared under the same conditions. The samples in Fig. 2 were synthesized using unsieved precursor powder for SPS in order to reduce porosity. We estimated κ_P by subtracting the estimated electronic thermal conductivity κ_E from the measured total thermal conductivity κ_{TOTAL}. κ_E is usually approximated by the Weidemann Franz (WF) law, $\kappa_E = L_0\sigma T$, where L_0 is the Lorenz number and σ ($= 1/\rho$) is the electrical conductivity. We found a typical carrier concentration of $\sim 10^{20}$ cm^{-3}

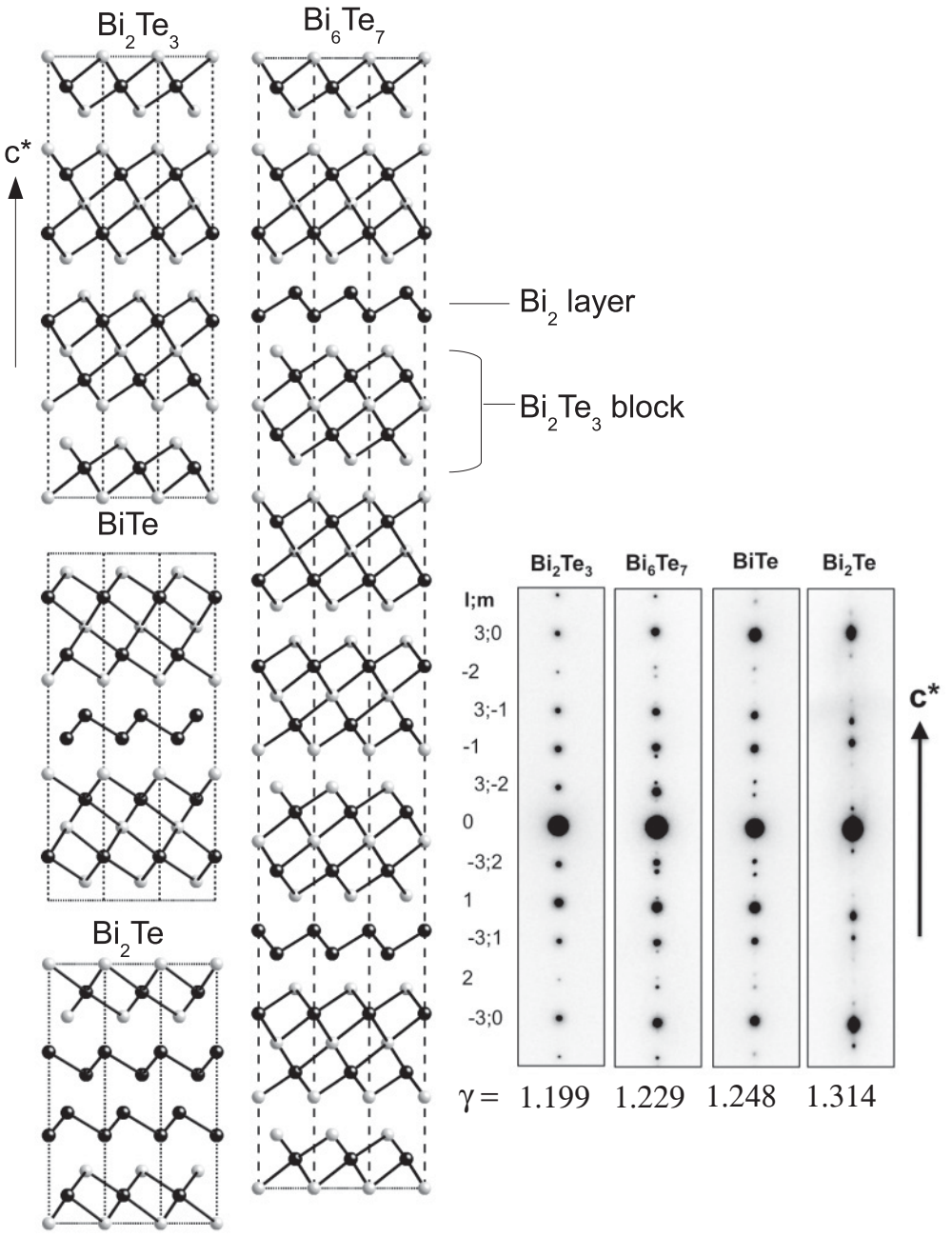

FIG. 1. Crystal structure of Bi_2Te_3, BiTe, Bi_2Te, Bi_6Te_7. These compounds are composed of Bi_2 layers and Bi_2Te_3 blocks, as confirmed by selected area diffraction patterns collected in a transmission electron microscope and powder x-ray diffraction (not shown). The parameter γ, which parametrizes the periodicity of each compound, agreed within one standard deviation of that found in previous diffraction studies of these materials. Other compounds of the form $(Bi_2)_m(Bi_2Te_3)_n$ exist but were not studied here.

in these alloys so that L_0 takes the Sommerfeld value of 2.44×10^{-8} W/K^2, appropriate for degenerate electron systems. Using the WF law and the measured ρ for each compound (Fig. 2, inset), $\kappa_P = \kappa_{TOTAL} - L_0\sigma T$ of the Bi_2-Bi_2Te_3 alloys appears significantly smaller for $T < 100$ K compared to Bi_2Te_3 and elemental Bi.[12] For $T > 200$ K and up to room temperature, κ_P increases with increasing T, likely due to bipolar thermal conduction that has not been estimated here. Radiation errors could also cause the apparent κ_P to increase with T above 200 K, but this error amounts to 10% or less at 300 K. In this work, we will focus on the $T < 100$ K behavior of κ_P where bipolar conduction and radiative losses are negligible.

In Fig. 2 we assumed that the WF law is a good approximation for κ_E. In conventional metallic materials, elastic scattering from defects affects the thermal and electric currents the same way so that the WF law is valid.[13] For electron-phonon scattering, the WF law no longer predicts κ_E when inelastic collisions involve phonons of a wave vector (q) much smaller than the Fermi wave vector (k_F).[14] Therefore in

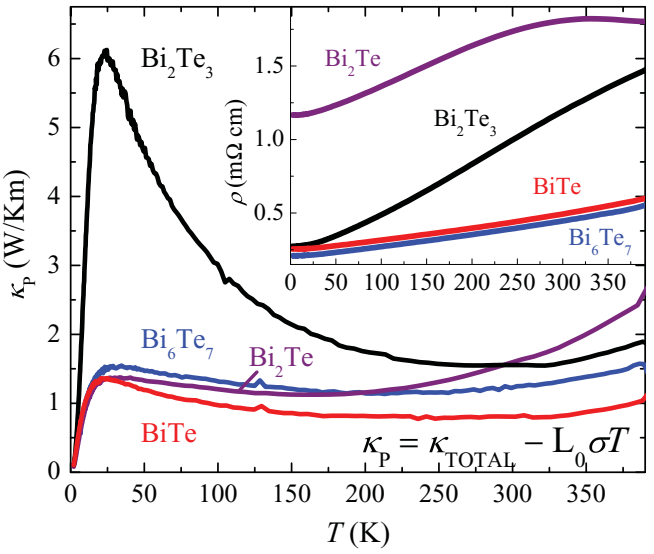

FIG. 2. (Color online) Phonon thermal conductivity of $(Bi_2)_m(Bi_2Te_3)_n$ alloys. BiTe, Bi_2Te, and Bi_6Te_7 have a reduced κ_P relative to Bi_2Te_3 below 100 K. We calculated κ_P using the Weidemann-Franz law and the measured electrical resistivity for each compound (inset).

order to judge if we have appropriately used the WF law, we must estimate the importance of small q phonons (relative to the magnitude of k_F).

The dominant phonon q is directly proportional to T. Phonons with $q \ll 2k_F$ will result in a violation of the WF law. In the Bi_2-Bi_2Te_3 alloys we have studied, carrier concentrations (n) are $\sim 10^{20}$ cm^{-3},[15] leading to an upper limit for $k_F \sim (3\pi^2 n)^{1/3} \sim 10^7$ cm^{-1}. The effective temperature below which electron-phonon scattering sets in for low carrier concentration systems (i.e., with $k_F \ll q_D$, the Debye wave vector) is given by $\theta^* = 2k_F v_S h/2\pi k_B$,[16] where v_S is the sound velocity, h is Planck's constant, and k_B is the Boltzmann constant. WF violations are therefore expected for $T \ll \theta^*$. Using the estimated k_F and an upper limit of $v_S \sim 2.85 \times 10^5$ cm/s reported for Bi_2Te_3 [17], $\theta^* \sim 56$ K. In As, which has $n \sim 10^{20}$ cm^{-3} (Ref. 16) and a maximum $v_S \sim 4.61 \times 10^5$ cm/s,[18] $\theta^* \sim 91$ K and $\kappa_E/\sigma T$ only deviates from L_0 (by at most -25%) below 10 K.[19] Thus in the Bi_2-Bi_2Te_3 alloys, we expect that the κ_P for 10 K $< T <$ 100 K reported in Fig. 2 almost entirely represents lattice thermal conduction.

The reduction of κ_P below 100 K does not systematically vary across the Bi_2-Bi_2Te_3 series [Fig. 3(a)], suggesting that the layered crystal structure shown in Fig. 1 does not play a direct role in this phenomenon. With increasing at. % Bi, both unit-cell size and the number of Bi bilayers change within the Bi_2-Bi_2Te_3 structure yet the peak in κ_P (e.g., κ_P is maximum, $\sim$1.4 W/Km, at 25 K in BiTe in Fig. 2) is constant within the error bars. The anisotropic crystal structure shown in Fig. 1 suggests that $(Bi_2)_m$-$(Bi_2Te_3)_n$ single crystals might have a larger in-plane to cross-plane κ_P ratio than that of Bi_2Te_3 [$\kappa_{11}/\kappa_{33} \sim 1.2$ at 100 K (Ref. 20)] due to the presence of Bi_2 bilayers. Furthermore, this κ_P anisotropy should change with Bi content. However, the materials measured in Fig. 2 were untextured polycrystals,

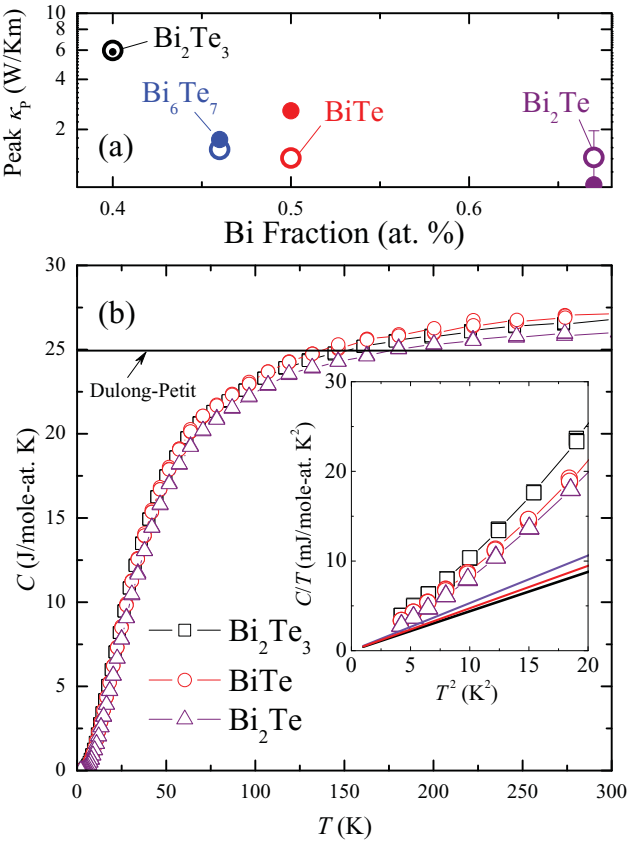

FIG. 3. (Color online) (a) The peak κ_P for Bi_6Te_7, BiTe, and Bi_2Te was reduced by factor of $\sim$3 compared to Bi_2Te_3, but did not change systematically with at. % Bi. Data were collected on samples made from unsieved (open symbols) and sieved (solid symbols) precursor powders. (b) The specific heat (C) for each compound was very similar indicating similar elastic properties. The low-temperature slope of C/T versus T^2 (inset), a measure of sound velocity, also had little variation. The small variation of this slope could be explained using effective-medium theory simulations (solid lines) for each compound by considering them as simple mixtures of Bi and Bi_2Te_3.

confirmed through EBSD measurements in a scanning electron microscope (SEM). In materials with an anisotropic thermal conductivity of $\kappa_{in-plane} > \kappa_{cross-plane}$, the averaging rule for a bulk polycrystal with randomly oriented grains is very close to that of a polycrystalline thin film giving the effective thermal conductivity as $(2\kappa_{in-plane} + \kappa_{cross-plane})/3$.[21] Given that these materials are polycrystals and that κ_P is independent of m for $m > 0$, we are likely measuring κ_{11} and that $\kappa_{11} > \kappa_{33}$. Thus Fig. 3(a) implies that the in-plane κ_P of these materials is significantly reduced compared to that of Bi_2Te_3 and of elemental Bi (e.g., $\kappa_P \sim 30$ W/K m at 60 K).[22]

Using calorimetry, we found no significant change in the specific heat at constant pressure (C) and thus the average sound velocity (v), which influences κ_P through the kinetic formula, $\kappa_P \propto Cvl$, where l is the phonon mean free path.[14] For all the compounds studied, C [Fig. 3(b)] is weakly T dependent near 300 K and close in magnitude to the Dulong-Petit value ($\sim$24.9 J/mole at. K). C then begins to decrease near 150 K for all these materials, suggesting that they all have similar Debye

temperatures (Θ_D). At low T, where $C \propto (T/\Theta_D)^3$ for phonons, we found little difference in the slope (inversely proportional to Θ_D) of C/T versus T^2 [Fig. 3(b), inset]. We compared the differences in slope of the C/T versus T^2 curves with that expected from considering these compounds as simple mixtures of Bi and Bi_2Te_3. Using the bounds on the elastic constants of mixtures, [23] the shear and bulk elastic moduli for Bi (Ref. 24) and Bi_2Te_3,[25] and assuming $v = \sqrt{G/\rho}$, where G is the bulk modulus, we estimated the change in $\Theta_D \propto v$,[26] given that $\Theta_D \approx 164$ K for Bi_2Te_3.[25] The slope of C/T versus T^2 simulated using this effective-medium approach for each material [solid lines, Fig. 3(b) inset] shows a variation comparable to that of the experimental data. Variations in v for $(Bi_2)_m(Bi_2Te_3)_n$ compounds are thus less than 10%, validated by considering this system as a mixture of Bi and Bi_2Te_3, and cannot explain the large observed reduction in κ_P.

We can eliminate several potential causes for the decrease of the in-plane κ_P in these alloys; a decreased sound velocity will decrease κ_P, but our C measurements reveal a small variation in average sound velocity across this series and implies that phonon scattering decreases κ_P. Note that sound velocity is averaged in a very similar way as thermal conductivity in specific-heat experiments on polycrystals.[27] Each sample had a very similar grain-size distribution (quantitative grain sizes are discussed in Sec. VI) as judged from qualitative optical microscopy. The porosity varied from ~2%–5% across this series, which cannot explain (e.g., using an effective-medium theory[28]) the observed large decrease in κ_P in Fig. 2. Furthermore, we prepared a set of samples with SPS using powder that passed through a 50-μm sieve but not a 25μm sieve in order to artificially increase porosity.[29] While the porosity of these sieved samples approximately doubled, κ_P remained unchanged. From these control experiments, we can rule out grain-boundary and porosity based mechanisms for phonon scattering. We therefore suggest that microscopic defects are the main source of phonon scattering in the $(Bi_2)_m$-$(Bi_2Te_3)_n$ compounds. In order to further identify a specific microscopic defect responsible for the low κ_P, a model for how defects affect phonon thermal transport must be compared to the experimental data.

VI. BOLTZMANN TRANSPORT ANALYSIS OF PHONON THERMAL CONDUCTIVITY

The influence of different defects on κ_P was studied using the Boltzmann equation for phonon transport. Using a combination of simulations and fitting, we were able to match the experimental data with the Boltzmann model and extract scattering rates for several kinds of defects. Finally, we validated the Boltzmann model fit by comparing the microstructural information implied by the scattering rates (e.g., grain size, dislocation density) with our own microscopy observations and those found in the literature. All computations were carried out using a custom code written in MATHEMATICA®.

We modeled the $(Bi_2)_m$-$(Bi_2Te_3)_n$ series using the Debye-Callaway approximation (DCA) of the Boltzmann transport equation.[30] In this approach, an integral equation for κ_P results after the relaxation time approximation is used to solve the linearized Boltzmann equation and a Debye spectrum is assumed for the phonons. This equation for κ_P then requires an expression for the scattering rate (τ^{-1}) in order to model experimental data. Analytical expressions for the scattering rate exist for many kinds of defects.

We parametrized the resistive τ^{-1} as follows:

$$\tau^{-1} = v/L + a\left(\hbar\gamma^2/Mv^2\theta\right)\omega^2 T e^{-\theta/3T} + b\left(V/4\pi v^3\right)\omega^4 + c\left(2\gamma^2 V^{1/3}/27v\right)\omega^2 + d\omega. \quad (1)$$

L, a, b, c, and d were adjustable parameters for scattering from grain or sample boundaries, umklapp phonon-phonon interactions, point defects, stacking faults, and dislocations, respectively. The symbols ω, v, γ, θ, M, and V represent acoustic-phonon frequency, sound velocity, Grüneisen constant, Debye temperature, average mass per atom, and average volume per atom, respectively, and were held fixed for the calculation. The forms for boundary, umklapp, and point defect scattering were taken from Ref. 31 and that for stacking fault scattering from Ref. 32. Reference 33 discusses the expression for dislocation scattering. The electron-phonon-scattering rate is ω linear in the degenerate limit,[30] and thus indistinguishable from dislocation scattering in this approach. M and V were calculated directly from the atomic masses and ratios of Bi and Te for each compound. θ and v varied by less than 10% for each compound according to C measurements [Fig. 3(b)]; this variation had a less than 1% effect on the calculation.

Separate scattering rates of the same form of Eq. (1) were included for longitudinal (L) and transverse (T) phonons by assuming different γ, θ, and v. The values $\gamma_L = 1$, $\gamma_T = 0.7$, $\theta_L = 96$ K, $\theta_T = 62$ K, $v_L = 2840$ m/s, and $v_T = 1590$ m/s were taken from Ref. 17. While θ used for the calculation was different from the polycrystalline averaged Θ_D determined from low T calorimetry,[25] we used the values from Ref. 17 because they were based on direct measurements of phonon frequencies at the zone boundary, resolved into L and T components.[34] The γ values of Ref. 17 did not agree with *ab initio* calculations,[35] where $\gamma_T \sim 1.17$ and $\gamma_L \sim 1.86$. Though Θ_D and γ varied in the literature, we used the Ref. 17 values since they resulted in an accurate model for the κ_P of Bi_2Te_3,[17] which could be used to systematically study the $(Bi_2)_m(Bi_2Te_3)_n$ series. As outlined in Ref. 31, the ratio of L to T phonon-scattering strengths was held constant. Similarly, normal phonon scattering was taken into account using the procedure in Ref. 31 and fixing the ratio of umklapp to normal scattering, keeping the adjustable parameters limited to L, a, b, c, and d.

We used simulation and curve fitting to model the samples in Fig. 2 with the DCA equation in order to determine which scattering mechanism(s) (inferred from adjustable parameters L, a, b, c, and d) best explains the low κ_P of the $(Bi_2)_m$-$(Bi_2Te_3)_n$ series. We found that curve fitting alone yielded ambiguous results. Nonlinear fitting schemes often converge to different final parameter sets with different initial conditions.[36] This occurs in many-parameter models because of the multiple shallow minima of the error function χ^2 (often normalized by the degrees of freedom, DOF) in parameter space. We overcame this problem using the following steps. First, we

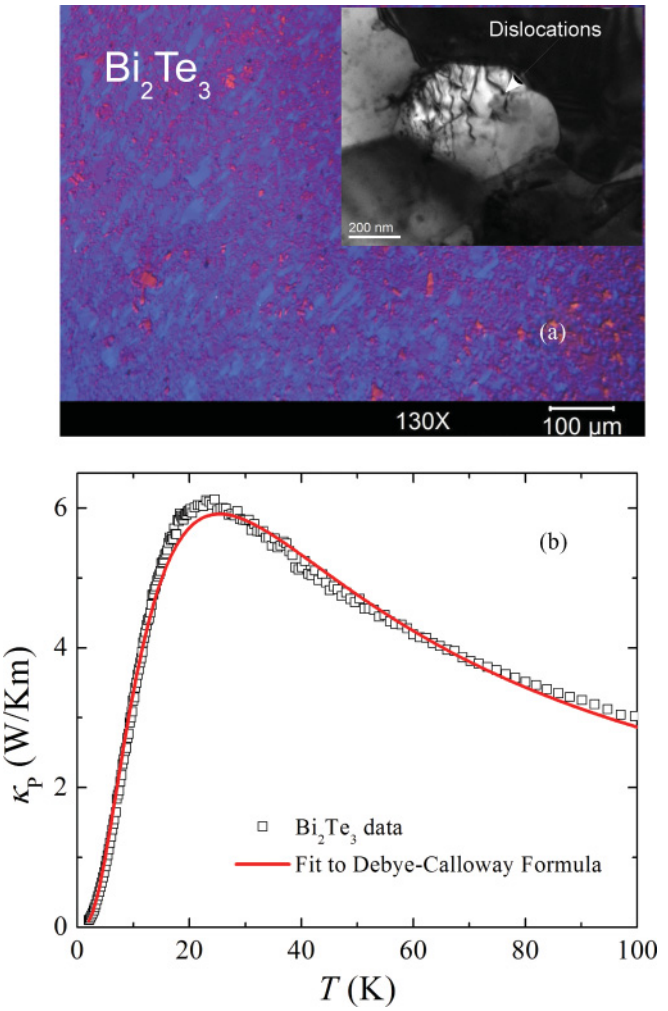

FIG. 4. (Color online) (a) Representative polarized optical micrograph of Bi_2Te_3 showing the grain-size distribution typical for all samples. Inset: Dark-field transmission electron micrograph of the same Bi_2Te_3 sample showing the presence of dislocations. We found no evidence of other kinds of extended defects. (b) The Debye-Callaway model (described in text) was fit (solid line) to the experimental Bi_2Te_3 κ_P data (open symbols). The fit parameters of this model were consistent with microstructural observations and previous fits to Bi_2Te_3 materials.

implemented the nonlinear fitting algorithm due to Transtrum,[37] which improves the convergence of the Levenberg-Marquadt method. Second, we performed a curve fit to the Bi_2Te_3 sample, validating the fit by comparing (when possible) the scattering rates to the microstructure. Finally, for each $m > 0$ sample, we ran simulations for κ_P by varying each scattering rate independently and comparing the results to the data. Each scattering rate has a distinct ω dependence, and therefore leads to a distinct T dependence for κ_P. This strategy allowed us to understand the relative importance of each scattering rate and to generate a variety of initial conditions for a formal curve fit. The different initial conditions led to different final parameter sets, so the best fit was that which yielded the lowest χ^2/DOF. We then checked these best-fit parameters against direct microstructural observations and microstructural information obtained from the literature.

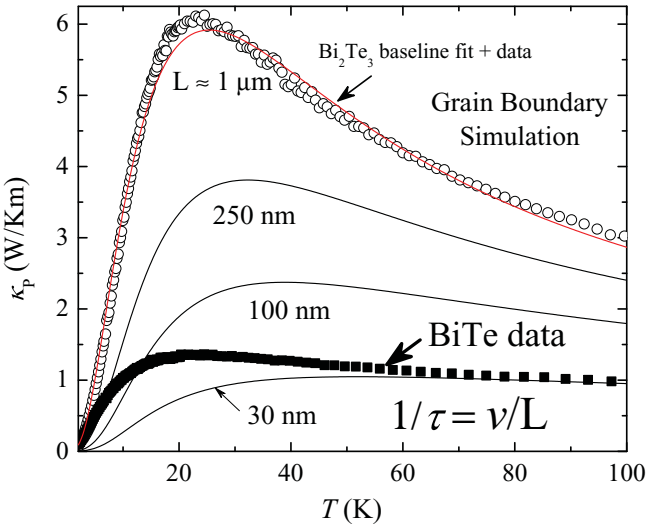

FIG. 5. (Color online) Debye Callaway model simulations (black lines) of grain-boundary scattering ($1/t = v/L$) for progressively smaller grain sizes (L) relative to the Bi_2Te_3 data/best fit (open circles/red line) as compared to experimental κ_P data for BiTe (closed squares). The remaining compounds were omitted for clarity. In order to reproduce the reduced κ_P at 100 K in BiTe relative to Bi_2Te_3, a hypothetical grain size of ~30 nm would be needed.

In Fig. 4, we fit the κ_P of Bi_2Te_3 to the DCA equation as just described and compared the results to microstructural observations. The main panel of Fig. 4(a) shows a representative optical micrograph for the Bi_2Te_3 sample. Using EBSD in an SEM to resolve individual grains based on their orientation, 70% of grains were less than 4 μm wide (ASTM grain size 21.1). We also conducted TEM observations to investigate the microstructure at higher spatial resolution. We found many grains with sizes in range of several hundred nanometers. We also observed extended dislocation networks in some of the grains. For instance, the inset of Fig. 4(a) shows a bright-field image of a grain of roughly 500 nm diameter. Several dislocations extend across the grain.

In Fig. 4(b), the best fit (solid line) is compared to the experimental κ_P for Bi_2Te_3. Five different starting parameter sets were generated, emphasizing each of the five scattering rates, and led to three distinct minima in χ^2. The fit with the lowest χ^2/DOF ($\approx$ 2.27) is shown in Fig. 4(b). The parameters found for the lowest χ^2 minimum are reported in Table I. The uncertainties in parameters were estimated using a Monte Carlo method.[38] The value for L (~0.93 μm) had the correct order of magnitude in comparison with our grain-size measurements (70% of grains < 4 μm wide). The magnitude of the umklapp scattering rate prefactor inferred from parameter a was comparable to that found from previous DCA fits to Bi_2Te_3 materials.[17]

The point defect parameter b ($\sim 9 \times 10^{-3}$) found from the present fit was between that expected for isotope scattering ($b \sim 8 \times 10^{-5}$, a negligible contribution) and an upper limit to alloy disorder in $(Bi,Sb)_2Te_3$ compounds ($b \sim 0.3$).[17] For disordered point defects involving two different species, $b = x(1-x)(\gamma_{mass} + \gamma_{bond})$, where x is the concentration of defects.[39] Point defect scattering of phonons occurs from

TABLE I. Best-fit parameters and goodness of fit (χ^2) normalized by the degrees of freedom (DOF) for the phonon thermal conductivity of Bi_2Te_3 within the Debye-Callaway model described in the text, parametrized according to Eq. (1). The parameters a, b, c, and d were dimensionless. Uncertainties in the parameters were generated from a Monte Carlo method, corresponding to $\Delta\chi^2/\mathrm{DOF} \approx 1$.

χ^2/DOF	L (μm) grain size	a umklapp	b point defects	c stacking faults	d dislocations
2.27	0.93	8.5	8.7×10^{-3}	1×10^{-4}	1.0×10^{-5}
Uncertainties $\Delta\chi^2/\mathrm{DOF} \approx 1$	0.05	0.1	0.4×10^{-3}	3×10^{-8}	3.5×10^{-9}

both mass and bond disorder. $\gamma_{\mathrm{mass}} = (\Delta M/M)^2$, where $\Delta M = M_A - M_B$ between the two species A and B, and $M = xM_A + (1-x)M_B$. $\gamma_{\mathrm{bond}} = \varepsilon(\Delta\delta/\delta)^2$, where $\Delta\delta$ is the radius difference between host and impurity, δ is the radius of the host atom, and ε is an adjustable parameter on the order of 1–100. In $(Bi,Sb)_2Te_3$, $x \sim 0.5$ and the upper limit[17] for $b \sim 0.3$. Letting A = Bi and B = Sb, using the ionic radii[40] $\delta_{\mathrm{Sb}} = 0.76$ Å and $\delta_{\mathrm{Bi}} = 1.03$ Å, we found $\varepsilon \sim 10$. In PbTe, $\varepsilon \sim 65$.[41] Our Bi_2Te_3 sample was n type, with a carrier concentration of $\sim 3 \times 10^{19}$ cm^{-3}, implying an excess Te concentration of ~0.2%.[42] The excess Te enters the Bi_2Te_3 lattice by replacing Bi,[43] suggesting an antisite defect model for point defect scattering. A value of $b \sim 9 \times 10^{-3}$, using $\varepsilon \sim 10$ with the atomic masses for Bi/Te and ionic radii[40] $\delta_{\mathrm{Bi}} = 1.03$ Å and $\delta_{\mathrm{Te}} = 2.21$ Å, yields a point defect concentration of ~0.27%, close to the excess Te concentration expected from the observed carrier concentration.

The parameter c for stacking fault scattering represents the number of stacking faults per layer.[32] In Bi_2Te_3, a value of $c \sim 1 \times 10^{-4}$ corresponds to about one stacking fault every 6 μm. This low stacking fault density is difficult to observe in a TEM experiment. We found no evidence for stacking faults originating from structural shifts of the lattice. High-resolution imaging is needed to detect stacking faults due to compositional shifts in the lattice, but was not performed here. Other two-dimensional (2D) surfaces may also contribute to phonon scattering in the same way as stacking faults. For example, we have found twin boundaries representing a reversal of the basal plane stacking sequence of the Bi_2Te_3 structure in ths material.[44] The strain field around a grain boundary may also partly contribute to $\tau^{-1} \sim \omega^2$ scattering. While twin and grain boundaries may have similar ω dependent phonon scattering, the scattering magnitude could be very different.

For dislocation scattering, $\tau^{-1} = N_i\Gamma_0\omega$,[33] where N_i is the dislocation density, $\Gamma_0 \sim \gamma^2B^2$, and B is the Burgers vector for the type of dislocation observed. For $d \sim 10^{-5}$, $\gamma \sim 1$ and b $\sim 10^{-10}$ m, we compute $N_i \sim 10^{15}$ m^{-2}. From the literature, we found $N_i \sim 10^6$ m^{-2} for single-crystal Bi_2Te_3,[45] and $\sim 10^{13}$ m^{-2} for commercial large grain Bi_2Te_3 based materials.[46] The order of magnitude for N_i for the small grain in Fig. 4(a) imaged with TEM is $\sim 10^{14}$ m^{-2}. Microstructural observations thus qualitatively agreed with the best fit and validated our approach for fitting data using the DCA.

Having validated the DCA approach for our Bi_2Te_3 sample using microstructural information, we performed simulations and curve fits for the $(Bi_2)_m(Bi_2Te_3)_n$ compounds. Starting from the baseline Bi_2Te_3 fit, each parameter was adjusted independently to match the magnitude of κ_P at 100 K. Simulations for BiTe are shown in Fig. 5 for progressively smaller grain sizes. According to Fig. 5, a grain size of nearly 30 nm is needed to match the magnitude of κ_P near 100 K, assuming the remaining parameters were the same as for Bi_2Te_3. In Fig. 6, we show the simulations for the rest of the scattering fit parameters for BiTe along with the observed κ_P shown in Fig. 2. The simulations for the remaining compounds (omitted for clarity) showed the same result. Figures 5 and 6 suggest that changing either stacking fault or point defect scattering parameters, while keeping the rest of the parameters fixed at their Bi_2Te_3 baseline values, captures the T dependence of κ_P for the $(Bi_2)_m(Bi_2Te_3)_n$ compounds. From the simulations, five different initial conditions were generated and then input into the fitting algorithm. These initial conditions did not all converge to the same final fit parameters. The "best fit" parameters reported for each compound in Table II were those that resulted in the lowest χ^2/DOF. Parameter uncertainties, generated in the same way as in Table I, were <1% for $\Delta\chi^2/\mathrm{DOF} \sim 1$.

According to the best-fit parameters for each compound (Table II), point defects are the largest contributor to phonon scattering that resulted in the reduced κ_P relative to Bi_2Te_3. The values for grain size, umklapp, stacking fault, and

TABLE II. Best-fit parameters for Bi_2Te, BiTe, and Bi_6Te_7 compared to Bi_2Te_3 as reported in Table I. The uncertainties in parameters were generated in the same way as for Bi_2Te_3 and were 1% or less. The point defect scattering rate increased an order of magnitude for the $(Bi_2)_m(Bi_2Te_3)_n$ series compared to Bi_2Te_3. The remaining scattering rates remained constant to within 10%.

Sample	L (μm) grain size	a umklapp	b point defects	c stacking faults	d dislocations
Bi_2Te_3	0.93	8.5	8.7×10^{-3}	1×10^{-4}	1×10^{-5}
Bi_2Te	0.76	7.68	0.16	1×10^{-4}	1×10^{-5}
BiTe	1.211	9.85	0.2	1×10^{-4}	1×10^{-5}
Bi_6Te_7	0.838	7.9	0.137	1×10^{-4}	1×10^{-5}

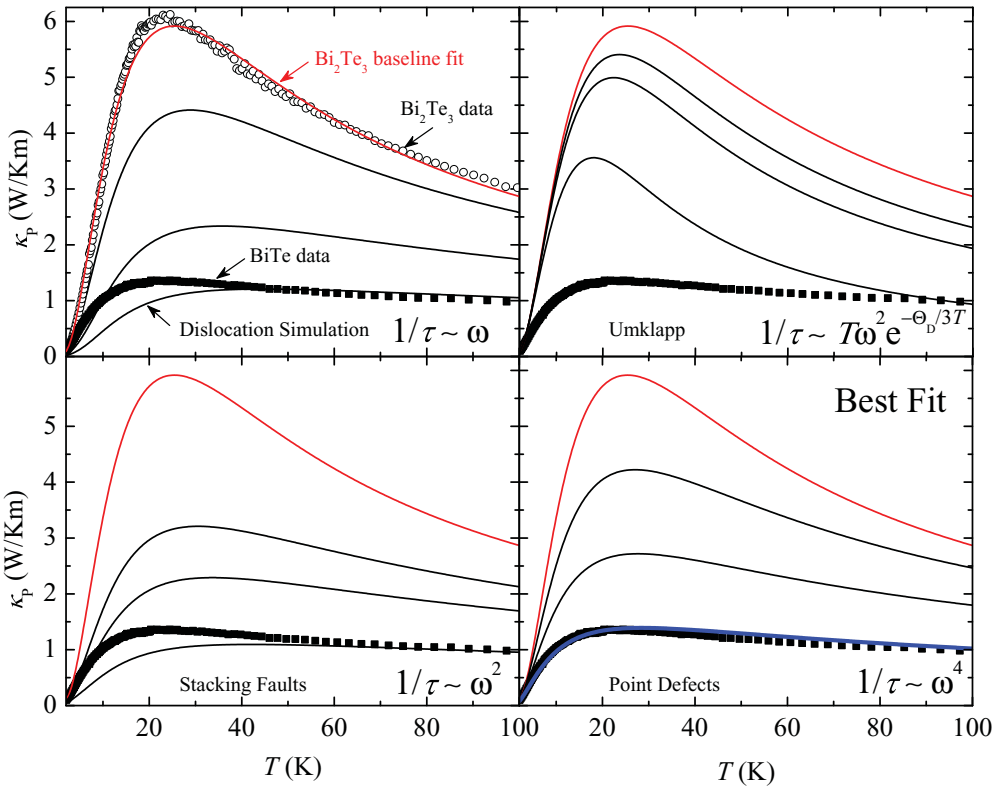

FIG. 6. (Color online) Debye Callaway simulations (solid lines) of the phonon thermal conductivity for dislocation, umklapp, stacking fault, and point defect scattering, as compared to the experimental data (solid symbols, only BiTe shown for clarity). For each panel, one scattering rate was increased while the remaining rates were kept fixed at their Bi_2Te_3 values obtained from curve fitting (red lines). Independently adjusting point defect scattering (blue line) closely matched the experimental data for all $(Bi_2)_m(Bi_2Te_3)_n$ samples for $m > 0$, and resulted in the best fit to the Debye Callaway equation for κ_P.

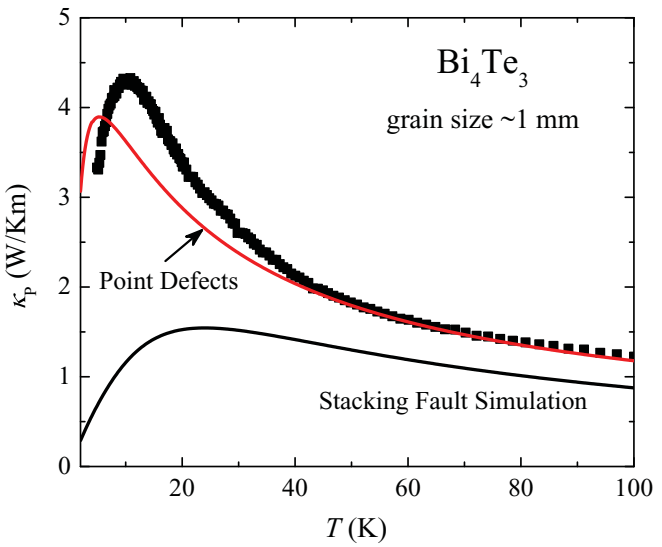

FIG. 7. (Color online) Point defect (red line) and stacking fault (black line) simulations compared to the phonon thermal conductivity of a Bi_4Te_3 sample with large (~1 mm) grains. In these simulations, the stacking fault and point defect scattering rates were kept the same as those for BiTe (lower left and right panel, respectively, of Fig. 6), while the grain size was increased to 1 mm. Point defect scattering more accurately captures the experimental κ_P.

dislocation scattering were unchanged within an order of magnitude compared to Bi_2Te_3 across the series. From optical microscopy, the grain-size distribution was qualitatively the same for Bi_2Te_3 and each Bi_2-Bi_2Te_3 compound. The point defect scattering rate changed by an order of magnitude compared to Bi_2Te_3. Point defect scattering did not change systematically across BiTe, Bi_2Te, and Bi_6Te_7, but this is just a quantitative way of expressing the conclusions based on Fig. 3(a) discussed in Sec. V.

Our simulations showed that differences between stacking fault and point defect scattering were more apparent at large grain sizes. This larger difference occurs because at larger grain sizes more stacking fault and point defect scattering events will occur per grain. A sample with larger grain size will then help validate the conclusion that point defects were more important than stacking faults in the DCA model for these materials. We synthesized a large grain (~1 mm, confirmed by optical microscopy) sample of a separate member of this series, Bi_4Te_3, and compared its measured κ_P to our DCA model. By measuring large grained Bi_4Te_3 instead of the compounds in Fig. 2, we could also test the conclusion from curve fitting that point defect scattering did not change with Bi content. Figure 7 shows the experimental κ_P for Bi_4Te_3 compared to two different simulations. We took the simulations for stacking faults and point defects shown in Fig. 6 and manually changed

the grain size to 1 mm, keeping the rest of the parameters fixed. Figure 7 shows that the point defect simulation comes much closer to the experimental κ_P than that for stacking fault scattering. Our conclusions based on curve fitting thus apply to a separate $(Bi_2)_m(Bi_2Te_3)_n$ sample with much larger grain size prepared by a very different method. This experiment also supports the idea that the point defects are intrinsic in these materials since the sample measured in Fig. 7 was annealed for a week at 400 C, which should eliminate nonequilibrium defects.

From Table II, we found $b \approx 0.2$ (Table II) for the $(Bi_2)_m$-$(Bi_2Te_3)_n$ series, nearly 20 times larger than that found for Bi_2Te_3. These compounds have not been doped in any way so we need not consider alloy scattering amongst three elements. If the source of disorder implied by the larger value of b in Table II is vacancies, then $\Delta M/M = \Delta\delta/\delta \approx -1$ and $b \sim x(1-x)(1+\varepsilon)$. Using $\varepsilon \sim 10$ as for Bi_2Te_3, we found a (Bi or Te) vacancy concentration of ~1.9%. Using the same masses and ionic radii of Bi/Te discussed previously for point defect scattering in Bi_2Te_3, a value of $b \approx 0.2$ yields an antisite defect concentration of ~1.6% when Te substitutes Bi, but ~6.1% when Bi substutites for Te. The $(Bi_2)_m$-$(Bi_2Te_3)_n$ series occur as line compounds and should not contain excess Te as in Bi_2Te_3. The ~2% point defect concentration is ten times larger than that found for Bi_2Te_3.

VII. CONCLUSIONS

We have shown that the phonon thermal conductivity in $(Bi_2)_m$-$(Bi_2Te_3)_n$ is significantly lower than that of Bi_2Te_3 and elemental Bi below 100 K. The thermal conductivity measurements were dominated by the in-plane κ_P due to the polycrystalline nature of our samples. The lowered κ_P was likely due to static defects rather than the unusual crystal structure. Using the DCA model, we established that the low κ_P originates from point defect scattering and since these materials are not doped the point defects must be either vacancies or antisite defects. While κ_P is low below 100 K for these compounds, they do not have an improved thermoelectric figure of merit relative to Bi_2Te_3 because the added Bi renders them semimetals, reducing the Seebeck coefficient by more than half.[7] More interesting was the evidence that there may be large (~2%) concentrations of point defects, an order of magnitude beyond that found for Bi_2Te_3. The point defects were present in samples prepared by two different methods, one of which involved annealing the specimen for a week close to the melting temperature. High-temperature annealing removes nonequilibrium defects, so we believe that the point defects inferred from κ_P measurements are intrinsic to these materials. Further experiments are needed to confirm the presence and identity (e.g., vacancy versus antisite) of point defects, since they cannot be probed using conventional TEM, as presented here.

ACKNOWLEDGMENTS

Sandia is a multiprogram laboratory operated by Sandia Corporation, a Lockheed Martin Company, for the U.S. Department of Energy's National Nuclear Security Administration under Contract No. DE-AC04-94AL85000. Work at Sandia was supported by the LDRD program. The work at Clemson University was supported by DOE/EPSCoR Implementation Grant No. DE-FG02-04ER-46139 and the SC EPSCoR cost sharing program. We acknowledge M. Transtrum for assistance with nonlinear curve fitting, S. McCall for providing machine time for calorimetry measurements, M. Homer for technical assistance, and J. D. Sugar for sharing TEM observations in Bi_4Te_3. A.L.L.S. acknowledges the hospitality of Clemson University and Sandia National Laboratories. We thank J. D. Sugar and C. D. Spataru for helpful comments.

[1] G. Mahan, Solid State Phys. **51**, 81 (1997).
[2] G. J. Snyder and E. S. Toberer, Nat. Mater. **7**, 105 (2008).
[3] D. T. Morelli, V. Jovovic, and J. P. Heremans, Phys. Rev. Lett. **101**, 035901 (2008).
[4] G. A. Slack, J. Phys. Chem. Solids **34**, 321 (1973).
[5] D. P. Spitzer, J. Phys. Chem. Solids **31**, 19 (1970).
[6] H. Okamoto and L. E. Tanner, *Bi-Te Phase Diagram*, edited by P. Villars, H. Okamoto, and K. Lenzual (ASM International, Materials Park, OH, 2006).
[7] J. W. G. Bos, H. W. Zandbergen, M. H. Lee, N. P. Ong, and R. J. Cava, Phys. Rev. B **75**, 195203 (2007).
[8] I. Terasaki, Y. Sasago, and K. Uchinokura, Phys. Rev. B **56**, R12685 (1997).
[9] K. Koumoto, H. Koduka, and W.-S. Seo, J. Mater. Chem. **11**, 251 (2001).
[10] H. Böttner, G. Chen, and R. Venkatasubramanian, MRS Bull. **31**, 211 (2006).
[11] B. D. Cullity and S. R. Stock, *Elements of X-Ray Diffraction*, 3rd ed. (Prentice-Hall, Englewood Cliffs, NJ, 2001).
[12] C. F. Gallo, B. S. Chandrasekhar, and P. H. Sutter, J. Appl. Phys. **34**, 144 (1963).
[13] N. Ashcroft and N. D. Mermin, *Solid State Physics* (Saunders, Philadelphia, 1976).
[14] J. Ziman, *Electrons and Phonons: The Theory of Transport Phenomena in Solids* (Oxford University Press, New York, 2001).
[15] Carrier concentrations were esimated using low magnetic-field Hall effect measurements and were weakly T dependent.
[16] J. Issi, Aust. J. Phys. **32**, 585 (1979).
[17] C. Chiritescu, C. Mortensen, D. G. Cahill, D. Johnson, and P. Zschack, J. Appl. Phys. **106**, 073503 (2009).
[18] N. G. Pace, G. A. Saunders, and Z. Sümengen, J. Phys. Chem. Solids **31**, 1467 (1970).
[19] J. Heremans *et al.*, J. Phys. C **10**, 4511 (1977).
[20] H. Kaibe, Y. Tanaka, M. Sakata, and I. Nishida, J. Phys. Chem. Solids **50**, 945 (1989).
[21] F. Yang, T. Ikeda, G. J. Snyder, and C. Dames, J. Appl. Phys. **108**, 034310 (2010).
[22] J. Boxus, C. Uher, J. Heremans, and J. P. Issi, Phys. Rev. B **23**, 449 (1981).
[23] Z. Hashin and S. Shtrikman, J. Mech. Phys. Solids **11**, 127.
[24] Y. Eckstein, A. W. Lawson, and D. H. Reneker, J. Appl. Phys. **31**, 1534 (1960).

[25]J. O. Jenkins, J. A. Rayne, and R. W. Ure, Phys. Rev. B **5**, 3171 (1972).
[26]$\Theta_D \propto v n_A^{1/3}$, but n_A changes by less than 10% across the entire $(Bi_2)_m$-$(Bi_2Te_3)_n$ series.
[27]O. L. Anderson, J. Phys. Chem. Solids **24**, 909 (1963).
[28]R. M. Costescu, A. J. Bullen, G. Matamis, K. E. O'Hara, and D. G. Cahill, Phys. Rev. B **65**, 094205 (2002).
[29]J. Reed, *Principles of Ceramic Processing* (Wiley and Sons, New York, 1995).
[30]R. Berman, *Thermal Conduction in Solids* (Oxford University Press, New York, 1976).
[31]D. T. Morelli, J. P. Heremans, and G. A. Slack, Phys. Rev. B **66**, 195304 (2002).
[32]P. Klemens, Can. J. Phys. **35**, 441 (1957).
[33]K. Ohashi, J. Phys. Soc. Jpn. **24**, 437 (1968).
[34]V. Wagner, G. Dolling, B. M. Powell, and G. Landweher, Phys. Status Solidi B **85**, 311 (1978).
[35]B.-L. Huang and M. Kaviany, Phys. Rev. B **77**, 125209 (2008).
[36]W. H. Press, S. A. Teukolsky, W. T. Vetterling, and B. P. Flannery, *Numerical Recipes in C. The Art of Scientific Computing* (Cambridge University Press, Cambridge, 1992).
[37]M. K. Transtrum, B. B. Machta, and J. P. Sethna, Phys. Rev. Lett. **104**, 060201 (2010).
[38]J. S. Alper and R. I. Gelb, J. Phys. Chem. **94**, 4747 (1990).
[39]B. Abeles, Phys. Rev. **131**, 1906 (1963).
[40]R. D. Shannon and C. T. Prewitt, Acta Crystallogr., Sect. B **26**, 1046 (1970).
[41]G. Alekseeva, B. Efimova, L. Ostrovskaya, O. Serebryannikova, and M. Tsypin, Sov. Phys. Semicond. **4**, 1122 (1971).
[42]C. B. Satterthwaite and R. W. Ure, Phys. Rev. **108**, 1164 (1957).
[43]G. R. Miller and C.-Y. Li, J. Phys. Chem. Solids **26**, 173 (1965).
[44]D. L. Medlin, Q. M. Ramasse, C. D. Spataru, and N. Y. C. Yang, J. Appl. Phys. **108**, 043517 (2010).
[45]A. G. Kunjomana and E. Mathai, J. Mater. Sci. **26**, 6171 (1991).
[46]D. Eyidi, D. Maier, O. Eibl, and M. Westphal, Phys. Status Solidi A **187**, 585 (2001).